Competing interactions in artificial spin chains

V.-D. Nguyen, Y. Perrin, S. Le Denmat, B. Canals, and N. Rougemaille
CNRS, Institut NEEL, F-38000 Grenoble, France
and Université Grenoble Alpes, Institut NEEL, F-38000 Grenoble, France
(Received 15 March 2017; revised manuscript received 7 June 2017; published 5 July 2017)

The low-energy magnetic configurations of artificial, frustrated classical spin chains are investigated using magnetic force microscopy and micromagnetic simulations. Contrary to most studies on two-dimensional artificial spin systems in which frustration arises from the lattice geometry, here magnetic frustration originates from competing interactions between neighboring spins. By tuning continuously the strength and sign of these interactions, we show that different magnetic phases can be stabilized. Comparison between our experimental findings and predictions from the one-dimensional anisotropic next-nearest-neighbor Ising model reveals that artificial frustrated spin chains have a richer phase diagram than initially expected. In addition to the observation of several magnetic orders and the potential extension of this work to highly degenerated artificial spin chains, our results suggest that the micromagnetic nature of the individual magnetic elements allows for the observation of metastable spin configurations.

DOI: 10.1103/PhysRevB.96.014402

Artificial spin ices are classical spin systems that were introduced about a decade ago [1,2] as a powerful way to explore frustrated magnetism experimentally, in a controlled manner [3]. First designed to investigate the rich physics of spin ice materials [4], they offer the advantage of being tunable at will. In addition to their tunability, one of the main reasons for fabricating artificial spin ice systems is the capability to spatially resolve their spin configurations using magnetic imaging techniques. This allows us to visualize in real space collective magnetic phenomena often associated with highly frustrated magnets [5]. For instance, artificial spin ice systems provide evidence of classical spin liquid states [6–9], Coulomb phases [10], complex magnetic ordering [11–13], charge crystallization [7,14–17], monopole-like excitations [18–21], and spin fragmentation [22].

Due to their correspondence with natural spin ice materials, most of the studies performed so far on artificial spin ice systems have focused on two-dimensional square [2,10,17,20,21,23–26] and kagome [1,6–9,14–19,22] geometries. In these artificial spin systems, the magnetic moments are Ising-like variables lying within the lattice plane and pointing locally along the angle bisectors of the checkerboard and kagome lattices, respectively. Because the interaction between nearest neighbors is ferromagnetic, the frustration in the artificial square and kagome spin ices is of geometrical origin: the system is not able to satisfy all its pairwise magnetic interactions simultaneously because of the lattice geometry that propagates conflicting information.

Here, we explore the low-energy magnetic states of artificial, classical spin chains in which frustration is not induced by the underlying geometry, but instead by competing interactions between neighboring elements. To do so, we follow the strategy developed for artificial Ising chains, where a series of magnetic islands are coupled through magnetostatics [27–30], and we combine it with the idea proposed for the uniaxial triangular [31,32] and square [33] Ising lattices to impose competing interactions. More specifically, we use the angular dependence of the dipolar interaction to tune the sign and strength of the coupling between neighboring nanomagnets.

To illustrate the influence of the angular dependence of the dipolar interaction, we first consider two (classical) magnetic moments $\vec{\mu}_i$ and $\vec{\mu}_j$ having an Ising-type degree of freedom, separated by a distance r_{ij} [see Fig. 1(a), where the Ising spins point along the y direction]. Depending on the angle between the y direction and the $\vec{r}_{ij}$ vector, the dipolar interaction favors either a parallel or an antiparallel alignment of the two magnetic moments, as shown in Fig. 1(b).

Based on this simple property, we fabricated artificial spin chains from in-plane magnetized, elongated nanomagnets [see Fig. 1(c)], interacting through magnetostatics. The aspect ratio of these nanomagnets is such that shape anisotropy determines the magnetization direction, so that each nanomagnet can be considered as an Ising pseudospin. By arranging these elongated nanomagnets on a unidimensional chain oriented along the x axis while shifting periodically half of the nanomagnets along the y direction, the coupling strength between nearest- (J_1) and next-nearest (J_2) neighbors can be controlled [see Figs. 1(d)–1(f)]. In particular, the vertical shift s [see Fig. 1(c)] allows a fine tuning of the J_1 coupling strength, both in amplitude and sign. For instance, the condition $s = 0$ gives rise to an antiferromagnetic coupling ($J_1 < 0$) between nearest neighbors [see Fig. 1(d)], while imposing $s = L$, where L is the length of the nanomagnets, leads to a ferromagnetic coupling ($J_1 > 0$) [see Fig. 1(e)]. Consequently, intermediate situations can be reached in which s is such that $J_1 = 0$ [see Fig. 1(f)] or $|J_1| = 2 \times |J_2|$, for example. This simple geometrical parameter s thus permits the investigation of different magnetic scenarios, and in particular cases in which interactions between neighboring nanomagnets compete. A comparison with predictions from the one-dimensional anisotropic next-nearest-neighbor Ising (ANNNI) model [34,35] can then done given the system Hamiltonian $H = -J_1 \sum_i \sigma_i \sigma_{i+1} + J_2 \sum_i \sigma_i \sigma_{i+2}$, where σ_i is an Ising variable (± 1) coding for the spin state of the magnetic moment residing on site i. Note that the magnetostatic interactions, coupling nearest- and next-nearest-neighboring nanomagnets through the J_1 and J_2 terms, respectively, are then described within the one-dimensional (1D) ANNNI model as pseudoexchange interactions.

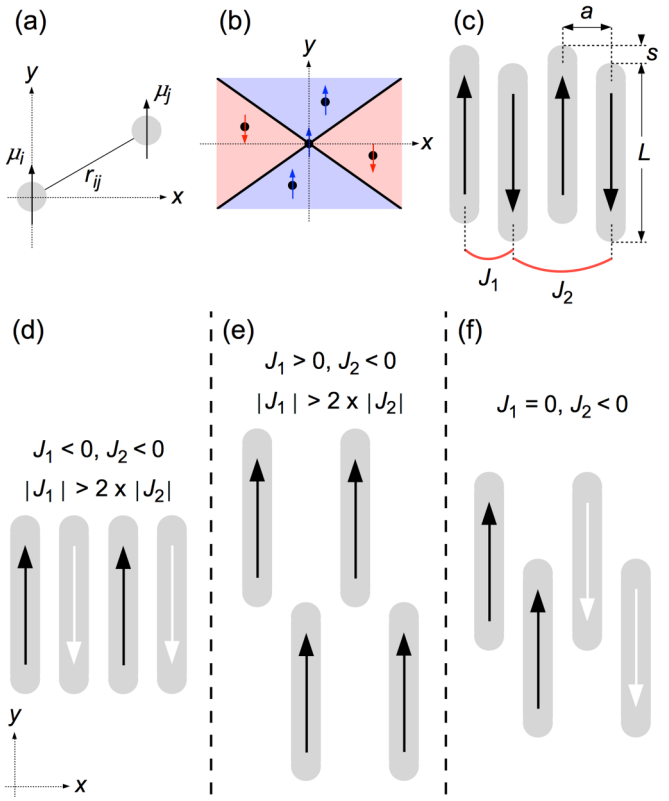

FIG. 1. (a) Schematics of two classical magnetic moments μ_i and μ_j pointing along the y axis and separated by a distance r_{ij}. (b) Diagram illustrating that the dipolar interaction favors ferromagnetic (blue region) or antiferromagnetic (red region) coupling between two magnetic moments depending on their relative position in the xy plane. (c). Schematics showing the different geometrical parameters and coupling strengths relevant in this work. (d)–(f) Different possible magnetic orders predicted by the one-dimensional ANNNI model depending on the relative strength of the coupling coefficients. $s = 0$ (d), $s = L$ (e), and $s < L$ (f). Arrows indicate the magnetization direction.

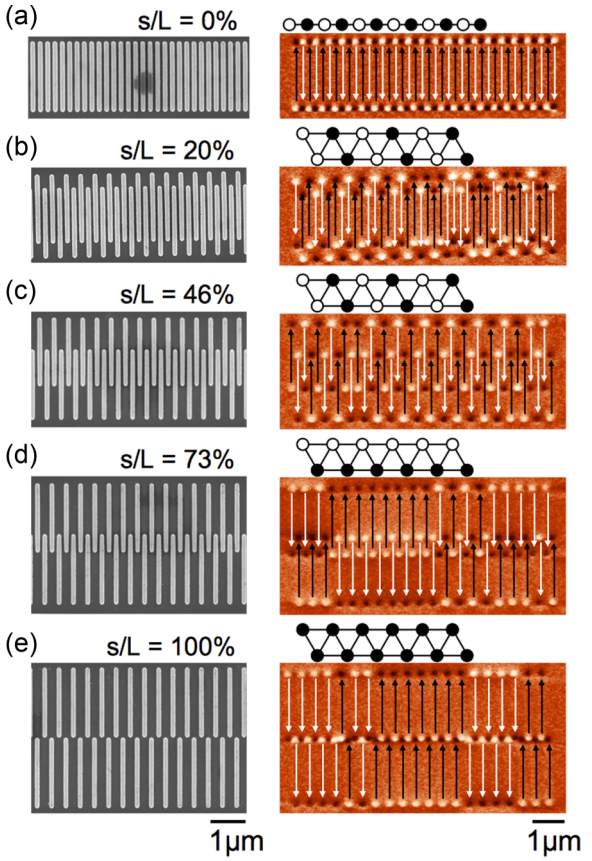

FIG. 2. SEM (left) and MFM (right) images of demagnetized spin chains for different values of the s/L ratio. On the MFM images, the magnetic contrast appears in black and white, while the black and white arrows indicate the local direction of magnetization deduced from this contrast. The sketches above the MFM images illustrate the expected ground-state configuration, where the black and white circles denote a spin pointing upward and downward, respectively. The three magnetic phases observed experimentally correspond to an antiferromagnetic ordering [(a) and (d)], an antiferromagnetic dimer state [(b) and (c)], and a ferromagnetic phase (e).

The spin chains were made of permalloy nanomagnets having typical dimensions of $150 \times 2250 \times 30\,\text{nm}^3$, i.e., with an aspect ratio of 15. To ensure a significant coupling strength between neighboring nanomagnets, the lattice parameter a [see Fig. 1(c)] was set to 225 nm, leading to a gap between two adjacent elements of only 75 nm. Each chain is composed of 40 nanomagnets, and the vertical shift s is varied from 0 to 2250 nm by steps of 150 nm. The chains have been patterned using e-beam lithography on a Si substrate. A 30-nm-thick permalloy film was subsequently deposited using e-beam evaporation and capped with 3 nm of Al to prevent the surface from oxidation. The chains were finally obtained using a conventional liftoff process. Figure 2 shows typical scanning electron microscopy (SEM) images of different chains.

Because of their typical dimensions, our artificial Ising pseudospins are classical athermal objects. Therefore, quantum and thermal effects play no role in our experiments: when a nanomagnet gets frozen in a given magnetic state, it remains in that state and never spontaneously fluctuates. To bring our spin chains into a low-energy magnetic configuration, the sample has been demagnetized using a long time field protocol. Essentially, and following previous works [36,37], an in-plane magnetic field is applied and ramped down from 250 mT to 0–80 h using an oscillating, linearly damped current in an electromagnet while rotating the sample at a frequency of about 10 Hz. To test the efficiency of our demagnetization protocol, we also repeated the experiment without rotating the sample and aligning the long axis of the nanomagnets with the field direction. Results (not shown) reveal qualitatively similar findings, although this second protocol is slightly less efficient in bringing the spin chains into a low-energy configuration. Room-temperature magnetic force microscopy (MFM) was then used to image the spin configurations of our demagnetized chains. Figure 2 shows typical MFM images for spin chains characterized by a shift of $s/L = 0\%$, 20%, 46%, 73%, and 100%. The black and white contrasts reveal the north and south poles of each nanomagnet. Magnetic contrast only appears at the two extremities of the nanomagnets, confirming their single magnetic domain state. From this contrast, each pseudospin can be unambiguously defined. We emphasize

that we never observe the presence of a domain wall within the nanomagnets, which are systematically found in a single domain state. Each nanomagnet can thus be considered as an Ising pseudospin, making our assemblies of nanomagnets purely one-dimensional Ising chains.

We first examine the case of unshifted spin chains ($s/L = 0\%$). Within a point dipole approximation, $J_1, J_2 < 0$ and $J_1 = 8 \times J_2$. We thus expect to observe from the one-dimensional ANNNI model an antiferromagnetic ordering of the artificial spin chains after the demagnetization protocol. Indeed, our MFM measurements reveal that the unshifted spin chains are in their ground state [Fig. 2(a)]. Although intuitive, this result is in fact surprising as perfect ordering is found over 40 spins. Despite the twofold degeneracy of the ground state, the spin chain was able to eliminate domain walls separating antiphase domains during the demagnetization protocol. This is in contrast with what was observed in other works where the correlation length was much smaller [27]. Our result is, however, similar to what was found in artificial spin chains where the ground-state degeneracy was intentionally broken [38] or when the shape of the nanomagnets was made asymmetric [28]. Thus, our protocol efficiently brings our artificial spin chains into their low-energy magnetic configurations.

We now study the influence of the vertical shift s on the magnetic configurations observed after demagnetization. Results are reported in Figs. 2(b)–2(e) for the four different ratios $s/L = 20\%$, 46%, 73%, and 100%. Spin chains made of fully shifted nanomagnets ($s/L = 100\%$) show large ferromagnetic domains separated by a few magnetic defects, i.e., magnetic domain walls [Fig. 2(e)]. In that case, if the first- and second-neighbor coupling strengths have opposite signs ($J_1 > 0$ and $J_2 < 0$), J_1 is larger in absolute value and imposes a ferromagnetic order. However, as we will see below, this result is surprising as it contradicts predictions from the 1D ANNNI model [35].

When the shift s is only slightly increased, however, an antiferromagnetic dimer phase (i.e., an alternating arrangement of two spins pointing upward and two spins pointing downward) is favored to accommodate contradictory information between neighboring elements. This is the case for the ratio $s/L = 20\%$ [Fig. 2(b)], where $J_1 \sim J_2 < 0$, consistently with what is expected from the 1D ANNNI model [35]. We note that the same magnetic configuration is obtained for a ratio s/L approaching 50%, where $J_1 \sim 0$ and $J_2 < 0$ [Fig. 2(c)]. This dimer phase would also be obtained for large shifts ($s \gg L$). In these two cases, J_1 becomes negligible compared to J_2, which remains unaffected by the vertical shift s. In other words, intermediate ($s/L \sim 50\%$) and large ($s \gg L$) shifts also lead to two antiferromagnetic, weakly coupled spin chains, thus forming an antiferromagnetic dimer phase, as expected from the one-dimensional ANNNI model [35].

Surprisingly, between the antiferromagnetic dimer phase and the ferromagnetic order, our spin chains exhibit a transition to an intermediate conventional antiferromagnetic state [Fig. 2(d)], similar to the one observed for unshifted spin chains [Fig. 2(a)]. The magnetic configuration is puzzling in the sense that the energy of the system is highly increased by the formation of head-to-head and tail-to-tail local configurations. As we will see below, we interpret the existence of this intermediate phase (like the ferromagnetic order) to be a signature of an out-of-equilibrium physics induced by the demagnetization protocol and the micromagnetic degree of freedom present at the nanomagnets' extremities.

Another way to visualize our experimental findings is to represent the nearest-neighbor spin-spin correlation function for all the spin chains we have fabricated. In particular, this quantity allows us to estimate how far a given configuration is from the expected ground state and how large is the shift window in which a given magnetic phase is observed experimentally. The nearest-neighbor spin-spin correlation coefficient is defined as $C_{\mathrm{NN}} = \langle \sigma_i \sigma_{i+1} \rangle$, where $\langle\,\rangle$ denotes the spatial average over the entire chain. Consequently, $C_{\mathrm{NN}} = -1$ corresponds to perfect antiferromagnetic order, while $C_{\mathrm{NN}} = +1$ represents ferromagnetic order. A zero C_{NN} value can be obtained if there are no spin-spin correlations in the system, or, more relevant to the present case, if an antiferromagnetic dimer phase is stabilized. Similarly, the next-nearest-neighbor spin-spin correlation coefficient is defined as $C_{\mathrm{NNN}} = \langle \sigma_i \sigma_{i+2} \rangle$.

The C_{NN} and C_{NNN} values deduced from the MFM images obtained after the demagnetization protocol (blue and green curves, respectively) are reported in Fig. 3(a). Four different regions can be identified depending on the s/L ratio, corresponding to the four magnetic states described above: a first antiferromagnetic state (light blue region), the antiferromagnetic dimer phase (light red region), a second antiferromagnetic state (in white), and the ferromagnetic order (light green region).

To interpret our results, we compare the magnetic phases obtained experimentally with those predicted by the 1D ANNNI model. To do so, we computed the J_1, J_2 coupling strengths using micromagnetic simulations [39] by comparing the energy of a pair of nanomagnets in a ferromagnetic (E_{FM}) and an antiferromagnetic (E_{AFM}) configuration, for different vertical shifts s. In other words, we compared two micromagnetic energies: $E_{\mathrm{FM}} = -J_1$ ($-J_2$), when the two considered nanomagnets, separated by one- (two-) chain parameter unit(s) a, are aligned ferromagnetically, and $E_{\mathrm{AFM}} = +J_1$ ($+J_2$) when the very same nanomagnets are aligned antiferromagnetically. Then, $E_{\mathrm{AFM}} - E_{\mathrm{FM}} = 2 \times J_1 (2 \times J_2)$ for nearest (next-nearest) neighbors. The mesh size was set to $1 \times 1 \times 30\,\mathrm{nm}^3$ to limit the effects from numerical roughness on the energy estimate. Material parameters are those commonly used for permalloy: $\mu_0 M_S = 1.0053$ T, $A = 10$ pJ/m, where M_S and A are the spontaneous magnetization and exchange stiffness, respectively. Magnetocrystalline anisotropy is set to zero. The results of the calculations are reported in Fig. 3(b), where the J_1/J_2 ratio is plotted as a function of s/L.

In the 1D ANNNI model, a magnetic transition is expected when the condition $|J_1/J_2| = 2$ is reached [35]: an antiferromagnetic configuration for $|J_1/J_2| > 2$ and an antiferromagnetic dimer state for $|J_1/J_2| < 2$. In Fig. 3(b), we thus identify two different regions. In light blue, $|J_1/J_2| > 2$, meaning that although both couplings favor an antiferromagnetic alignment of the nanomagnets, J_1 drives the ordering (antiferromagnetic state). In light red, $|J_1/J_2| < 2$, the situation is reversed, and J_2 drives the ordering (antiferromagnetic dimer phase). If our measurements are well described by the 1D ANNNI model

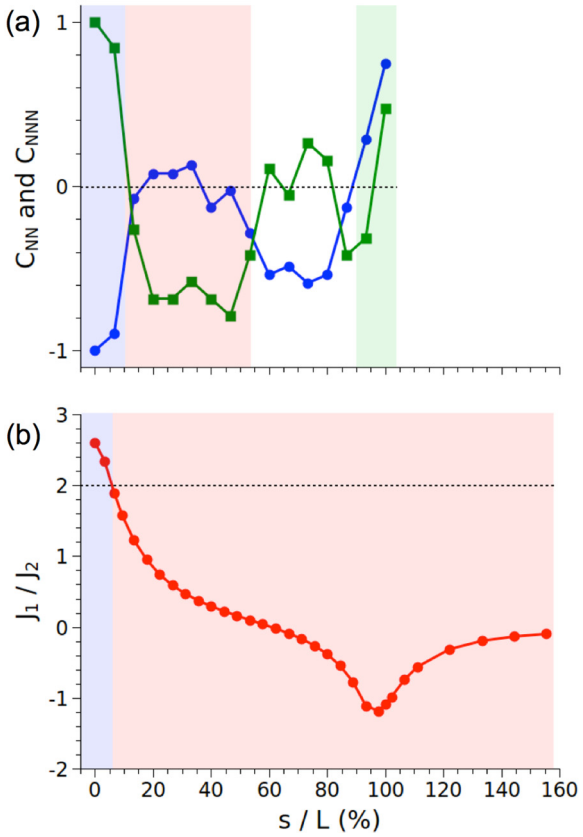

FIG. 3. (a) Nearest- (blue dots) and next-nearest- (green squares) neighbor spin-spin correlations as a function of the s/L ratio deduced from the MFM images reported in Fig. 2. (b) Ratio of the J_1 and J_2 coupling strengths as a function of s/L deduced from micromagnetic simulations. Colored regions in both graphs represent the magnetic configurations observed experimentally or expected from the one-dimensional ANNNI model: the antiferromagnetic order (light blue and white), the antiferromagnetic dimer phase (light red), and the ferromagnetic state (light green).

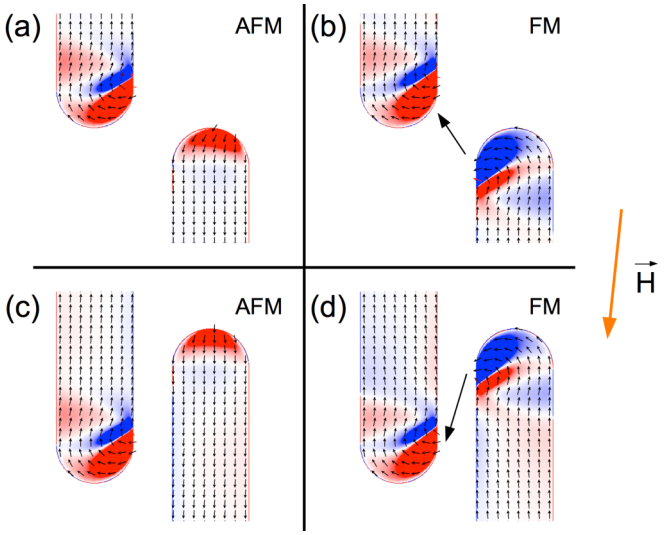

FIG. 4. Micromagnetic texture of two neighboring nanomagnets under an applied magnetic field (orange arrow) in four different configurations: for an antiferromagnetic and a ferromagnetic state when $s/L = 100\%$ (a),(b) and when $s/L = 80\%$ (c),(d), with $L = 2250$ nm. The black arrow in (b) and (d) indicates the dipolar field between the two nanomagnets. The red and blue contrast represents the divergence of the magnetization vector.

when $s/L < 50\%$, larger s/L ratios lead experimentally to two magnetic phases that are unexpected.

In the following, we thus investigate the origin of these unexpected antiferromagnetic (white region) and ferromagnetic (green region) phases. To do so, we performed micromagnetic simulations to determine at which applied external magnetic field a given nanomagnet is flipped depending on the magnetic configuration of one of its neighbors. The field required to initiate reversal is then determined for an antiferromagnetic and a ferromagnetic alignment of the two nanomagnets. To speed up convergence of the simulations, the damping parameter has been set to 1; the values deduced from the simulations then overestimate the real reversal fields. However, the purpose of these simulations is not to quantify the reversal field but rather to determine which of the two configurations is more stable under an applied external magnetic field.

Results are reported in Fig. 4 for two different cases: $s/L = 100\%$ [Figs. 4(a) and 4(b)] and $s/L = 80\%$ [Figs. 4(c) and 4(d)]. Although the two antiferromagnetic configurations [Figs. 4(a) and 4(c)] and the two ferromagnetic configurations [Figs. 4(b) and 4(d)] show strong similarities, the relative position of the nanomagnets' extremities has important consequences. When $s/L = 100\%$, the two nanomagnets aligned ferromagnetically [Fig. 4(b)] are coupled via a magnetostatic field (black arrow) that goes against the external applied field. Consequently, the total field felt locally by the two nanomagnets is weaker than the applied field, and additional energy is necessary compared to the antiferromagnetic configuration [Fig. 4(a)] in order to initiate magnetization reversal. The effect of this magnetostatic field has the opposite contribution when $s/L = 80\%$, and it increases the total magnetic field felt locally by the nanomagnets [Fig. 4(d)]. In that case, the magnetostatic field favors magnetization reversal, which occurs at an applied external field smaller than the one required in the antiferromagnetic configuration [Fig. 4(c)]. In other words, although the antiferromagnetic dimer state is the ground-state configuration in both cases ($s/L = 100\%$,80%), this ground state is destabilized during the demagnetization protocol due to the magnetostatic coupling between the local micromagnetic texture within two neighboring nanomagnets. When $s/L = 80\%$, a ferromagnetic configuration between neighboring elements is destabilized, and a conventional antiferromagnetic state is favored. When $s/L = 100\%$, the situation is reversed and a ferromagnetic alignment of neighboring nanomagnets is favored. This result highlights the role of micromagnetism and the limitation of the Ising pseudospin approximation, as already suggested in other works where the curling of the magnetization at the nanomagnets' extremities is supposed to impact spin-flip events [40,41].

To conclude, by tuning the vertical shift between neighboring nanomagnets arranged on a unidimensional chain, we observed magnetic configurations resulting from competing interactions. In addition to the antiferromagnetic state and the dimer phase expected from the one-dimensional ANNNI

model, we also evidenced a transition to an unexpected antiferromagnetic phase followed by a ferromagnetic state when the shift s becomes higher than 50%, typically. We believe that these two metastable states originate from the micromagnetic nature of the nanomagnets and the coupling of this additional magnetic degree of freedom with the applied external field during demagnetization. They are not expected in similar artificial spin chains that could be thermally activated. Our results also show that the condition $|J_1/J_2| = 2$ can be achieved experimentally, thus allowing an investigation of disordered and highly degenerated spin configurations in a one-dimensional classical spin system. Indeed, in that particular case, competing interactions destroy long-range order and lead, for large distances, to exponentially decaying spin-spin correlations superimposed with a spatial modulation [35]. It would be interesting to further explore such artificial, frustrated classical spin chains in order to test the extent to which the one-dimensional ANNNI model correctly described the physics we observed.

This work was partially supported by the Agence Nationale de la Recherche through Project No. ANR12-BS04-009 "Frustrated". The authors also thank the scientific staff of the Nanofab platform for the sample fabrication.

[1] M. Tanaka, E. Saitoh, H. Miyajima, T. Yamaoka, and Y. Iye, Phys. Rev. B **73**, 052411 (2006).
[2] R. F. Wang, C. Nisoli, R. S. Freitas, J. Li, W. McConville, B. J. Cooley, M. S. Lund, N. Samarth, C. Leighton, V. H. Crespi, and P. Schiffer, Nature (London) **439**, 303 (2006).
[3] C. Nisoli, R. Moessner, and P. Schiffer, Rev. Mod. Phys. **85**, 1473 (2013).
[4] M. J. Harris, S. T. Bramwell, D. F. McMorrow, T. Zeiske, and K. W. Godfrey, Phys. Rev. Lett. **79**, 2554 (1997).
[5] *Introduction to Frustrated Magnetism. Materials, Experiments, Theory*, edited by C. Lacroix, P. Mendels, and F. Mila (Springer, New York, 2009).
[6] Y. Qi, T. Brintlinger, and J. Cumings, Phys. Rev. B **77**, 094418 (2008).
[7] N. Rougemaille, F. Montaigne, B. Canals, A. Duluard, D. Lacour, M. Hehn, R. Belkhou, O. Fruchart, S. El Moussaoui, A. Bendounan, and F. Maccherozzi, Phys. Rev. Lett. **106**, 057209 (2011).
[8] L. Anghinolfi, H. Luetkens, J. Perron, M. G. Flokstra, O. Sendetskyi, A. Suter, T. Prokscha, P. M. Derlet, S. L. Lee, and L. J. Heyderman, Nat. Commun. **6**, 8278 (2015).
[9] O. Sendetskyi, L. Anghinolfi, V. Scagnoli, G. Moller, N. Leo, A. Alberca, J. Kohlbrecher, J. Luning, U. Staub, and L. J. Heyderman, Phys. Rev. B **93**, 224413 (2016).
[10] Y. Perrin, B. Canals, and N. Rougemaille, Nature (London) **540**, 410 (2016).
[11] S. Zhang, J. Li, I. Gilbert, J. Bartell, M. J. Erickson, Y. Pan, P. E. Lammert, C. Nisoli, K. K. Kohli, R. Misra, V. H. Crespi, N. Samarth, C. Leighton, and P. Schiffer, Phys. Rev. Lett. **109**, 087201 (2012).
[12] I. A. Chioar, N. Rougemaille, A. Grimm, O. Fruchart, E. Wagner, M. Hehn, D. Lacour, F. Montaigne, and B. Canals, Phys. Rev. B **90**, 064411 (2014).
[13] I. A. Chioar, N. Rougemaille, and B. Canals, Phys. Rev. B **93**, 214410 (2016).
[14] S. Zhang, I. Gilbert, C. Nisoli, G.-W. Chern, M. J. Erickson, L. O'Brien, C. Leighton, P. E. Lammert, V. H. Crespi, and P. Schiffer, Nature (London) **500**, 553 (2013).
[15] F. Montaigne, D. Lacour, I. A. Chioar, N. Rougemaille, D. Louis, S. M. Murtry, H. Riahi, B. S. Burgos, T. O. Mentes, A. Locatelli, B. Canals, and M. Hehn, Sci. Rep. **4**, 5702 (2014).
[16] I. A. Chioar, B. Canals, D. Lacour, M. Hehn, B. S. Burgos, T. O. Mentes, A. Locatelli, F. Montaigne, and N. Rougemaille, Phys. Rev. B **90**, 220407 (2014).
[17] J. Drisko, S. Daunheimer, and J. Cumings, Phys. Rev. B **91**, 224406 (2015).
[18] S. Ladak, D. E. Read, G. K. Perkins, L. F. Cohen, and W. R. Branford, Nat. Phys. **6**, 359 (2010).
[19] E. Mengotti, L. J. Heyderman, A. F. Rodrguez, F. Nolting, R. V. Hgli, and H.-B. Braun, Nat. Phys. **7**, 68 (2011).
[20] J. P. Morgan, A. Stein, S. Langridge, and C. H. Marrows, Nat. Phys. **7**, 75 (2011).
[21] C. Phatak, A. K. Petford-Long, O. Heinonen, M. Tanase, and M. DeGraef, Phys. Rev. B **83**, 174431 (2011).
[22] B. Canals, I. A. Chioar, V.-D. Nguyen, M. Hehn, D. Lacour, F. Montaigne, A. Locatelli, T. O. Mentes, B. S. Burgos, and N. Rougemaille, Nat. Commun. **7**, 11446 (2016).
[23] A. Farhan, P. M. Derlet, A. Kleibert, A. Balan, R. V. Chopdekar, M. Wyss, J. Perron, A. Scholl, F. Nolting, and L. J. Heyderman, Phys. Rev. Lett. **111**, 057204 (2013).
[24] J. P. Morgan, J. Akerman, A. Stein, C. Phatak, R. M. L. Evans, S. Langridge, and C. H. Marrows, Phys. Rev. B **87**, 024405 (2013).
[25] V. Kapaklis, U. B. Arnalds, A. Farhan, R. V. Chopdekar, A. Balan, A. Scholl, L. J. Heyderman, and B. Hjrvarsson, Nat. Nanotechnol. **9**, 514 (2014).
[26] J. M. Porro, A. Bedoya-Pinto, A. Berger, and P. Vavassori, New J. Phys. **15**, 055012 (2013).
[27] R. P. Cowburn, Phys. Rev. B **65**, 092409 (2002).
[28] A. Imre, G. Csaba, G. H. Bernstein, W. Porod, and V. Metlushko, Superlatt. Microstruct. **34**, 513 (2003).
[29] R. P. Cowburn and M. E. Welland, Science **287**, 1466 (2000).
[30] D. Li, C. Yu, J. Pearson, and S. D. Bader, Phys. Rev. B **66**, 020404(R) (2002).
[31] S. Zhang, J. Li, J. Bartell, X. Ke, C. Nisoli, P. E. Lammert, V. H. Crespi, and P. Schiffer, Phys. Rev. Lett. **107**, 117204 (2011).
[32] X. Ke, J. Li, S. Zhang, C. Nisoli, V. H. Crespi, and P. Schiffer, Appl. Phys. Lett. **93**, 252504 (2008).
[33] U. B. Arnalds, J. Chico, H. Stopfel, V. Kapaklis, O. Barenbold, M. A. Verschuuren, U. Wolff, V. Neu, A. Bergman, and B. Hjorvarsson, New J. Phys. **18**, 023008 (2016).
[34] S. Redner, J. Stat. Phys. **25**, 15 (1981).
[35] W. Selke, Phys. Rep. **170**, 213 (1988).
[36] X. Ke, J. Li, C. Nisoli, P. E. Lammert, W. McConville, R. F. Wang, V. H. Crespi, and P. Schiffer, Phys. Rev. Lett. **101**, 037205 (2008).
[37] R. F. Wang, J. Li, W. McConville, C. Nisoli, X. Ke, J. W. Freeland, V. Rose, M. Grimsditch, P. Lammert, V. H. Crespi, and P. Schiffer, J. Appl. Phys. **101**, 09J104 (2007).

[38] A. Imre, G. Csaba, L. Ji, A. Orlov, G. H. Bernstein, and W. Porod, Science **311**, 205 (2006).

[39] M. J. Donahue and D. G. Porter, OOMMF User's Guide, Version 1.0, Interagency Report NISTIR 6376, National Institute of Standards and Technology, Gaithersburg, MD (1999).

[40] K. Zeissler, S. K. Walton, S. Ladak, D. E. Read, T. Tyliszczak, L. F. Cohen, and W. R. Branford, Sci. Rep. **3**, 1252 (2013).

[41] N. Rougemaille, F. Montaigne, B. Canals, M. Hehn, H. Riahi, D. Lacour, and J.-C. Toussaint, New J. Phys. **15**, 035026 (2013).